Archives of Civil and Mechanical Engineering (2020) 20:20
https://doi.org/10.1007/s43452-020-00030-4

ORIGINAL ARTICLE

Comparative study of laser melting and pre-placed Ni–20% Cr alloying over nodular iron surface

N. Jeyaprakash[1,2] · Che-Hua Yang[1,2] · Muthukannan Duraiselvam[3] · S. Sivasankaran[4]

Received: 25 October 2019 / Accepted: 1 January 2020 / Published online: 21 February 2020

Abstract

In this study, two techniques such as laser surface melting (LSM) and laser surface alloying (LSA) were performed to protect the surface layers of nodular cast iron as it is used to manufacture different machine parts like cams, beds, camshafts, crankshafts, cylinders and engine blocks. The main objective of this research work is to examine the effects of LSM and LSA processes on phases, microstructure, hardness, wear resistance and surface roughness. The outcomes of both LSM and LSA specimens show a homogeneous structure, effective bonding of alloy powders with the base metal and crack-free surfaces. The hardness was improved 4 times (LSM) and 2.62 times (LSA) when compared with the base material. The tribological test shows improved wear resistance of LSM (8.82×10^{-7} kN) and LSA (1.32×10^{-6} kN) samples compared to the base material (4.36×10^{-6} kN). The examined wear tracks indicate that mild abrasion, adhesion and delamination were the major wear mechanisms. The reason for the enhancement of wear resistance is the refinement of microstructure, the solid solution strengthening effect and good bonding between alloy powders and base material. The LSM technique is a potential method to improve the tribological properties of industrial materials.

Keywords Laser surface melting · Laser surface alloying · Microstructure · Wear · Surface roughness

Abbreviations

NCI	Nodular cast iron
TIG	Tungsten inert gas
LSE	Laser surface engineering
LSM	Laser surface melting
LSA	Laser surface alloying
PVA	Polyvinyl alcohol
SEM	Scanning electron microscope
OM	Optical microscope
γ-Fe	Austenite
M-phase	Martensite phase
Fe_3C	Cementite
CoF	Coefficient of friction

✉ N. Jeyaprakash
prakash84gct@gmail.com; prakash@ntut.edu.tw

✉ S. Sivasankaran
sivasankarangs1979@gmail.com; sivasankaran@qec.edu.sa

Che-Hua Yang
chyang@ntut.edu.tw

Muthukannan Duraiselvam
durai@nitt.edu

1 Centre of Mass Customization Additive Manufacture, National Taipei University of Technology, Taipei, Taiwan, ROC

2 Institute of Manufacturing Technology, National Taipei University of Technology, Taipei, Taiwan, ROC

3 Department of Production Engineering, National Institute of Technology, Tiruchirappalli, India

4 Department of Mechanical Engineering, College of Engineering, Qassim University, Burayda 51452, Saudi Arabia

1 Introduction

The nodular cast iron (NCI) has different advantages such as good machinability, castability, high strength with less cost and thermal conductivity. The NCI has been used for the manufacture of different machine parts such as camshaft, crankshafts, cylinders, engine blocks and some mining equipment parts [1, 2]. However, during the continuous working conditions, their reliability and performance have been limited by different forms of wear. Previous studies reported that surface modification could improve the service life of the NCI components [3]. The wear resistance of cast iron was enhanced using high-energy processes such as electron beam, plasma spraying, thermal spraying, tungsten inert

gas (TIG) and lasers [4]. Further, the results stated that the thermally sprayed coatings exhibited the lower bond strength which made them unsuitable for wear resistance applications [5]. The conventional welding processes like the TIG arc welding have imparted the higher energy threshold and resulted in the formation of cracks because of the induced residual thermal stresses [6].

In recent years, laser-based surface treatment is considered being a suitable method to enhance the tribological properties. Higher re-solidification rates produced fine microstructure and unique properties that cannot be created by any other conventional method [7, 8]. Laser surface engineering (LSE) such as laser surface melting (LSM) and laser surface alloying (LSA) have been recognized as a promising technique compared to other methods [9]. In LSM, the top surface of the base metal melted and formed the fine homogeneous structure in a short time [10]. The rapid solidification and quenching process produced the fine microstructure with distinct properties. The higher cooling rates have advantages such as grain refinement, formation of amorphous structure, the extension of solid solubility and higher hardness. The LSM technique has been applied to some alloys such as stainless steel [11], carbon steel [12], Ni-based alloys [13], Al alloys [14] and the Ti alloys [15]. Noticeable changes were observed on LSM surfaces in terms of microstructure and improved properties.

In LSA, the hard alloy powders have been preplaced on the base material and passed through the laser source to fuse the alloy powders at some depth. The various hard powders such as Cr, Ni, Co, Fe, and W were used for the LSA. The LSA process can reach unique surface quality while maintaining the bulk material properties. The LSA process has less deformation which needs only minimum finishing work. The laser-alloyed top surface has good metallurgical bonding with the substrate producing fine microstructure. The laser-alloyed surfaces and machine parts can be tailored to specific requirements. Hence, the LSA is a new technique to reach a higher wear resistance with less cost [16]. Many investigators have concluded that the LSA is the best technique to enhance the wear resistance for Ti and Al alloys [17–19]. However, some limited research has focused on LSA and LSM on steel and cast iron material to improve the surface properties [20, 21]. But there is no comparative study of LSM and LSA on a NCI surface in terms of metallurgical, mechanical and tribological properties. In this study, LSM and LSA were performed to improve the WE of the NCI surface. In laser processing, a focused laser beam was emitted from the 3 kW fiber laser. The phase analysis, microstructure changes, hardness, wear resistance and surface roughness of both LSM and LSA samples were investigated, compared and reported.

2 Experimental

2.1 Samples and laser processing

Commercially available NCI is used as the base material with the dimensions of 25 × 25 × 30 mm. The base material surface was polished with various emery sheets to obtain a surface roughness of 10 µm. Table 1 shows the elemental composition of base material. Commercially available Ni with 20% Cr alloy powder was purchased from Oerlikon Metco, India. The purchased powder shows near-spherical and some irregular shape with a size of 20–100 µm as shown in Fig. 1a. After laser processing, specimens were cut into pin shape to dimensions of 6 × 6 × 30 mm. Figure 1b, c shows the schematic picture of laser processing and the photograph of laser material workstation, respectively. Polyvinyl alcohol (PVA) was purchased from Loba Chemie Pvt. Ltd, India, and mixed with deionized water and heated up to 320 °C. After, Ni–Cr powder was mixed with PVA and magnetically stirred for 2 h to make even mixing of alloy powder. Then evenly mixed alloy powders were preplaced on the base material surface until 200 µm thickness and kept in a fume cupboard for 48 h to dry the coating layers. Figure 1d shows the preplaced Ni–Cr coating with thickness. The prepared samples were laser processed with high-power fiber laser with a wavelength of 1080 nm (JK 3000FL, UK). Ar gas was used to avoid atmospheric contamination. Test coupons were exposed to various laser parameters to identify the optimal parameter. Table 2 shows the optimal laser parameter used in this study.

2.2 Wear study and characterization

After laser processing, the samples were cross-sectioned for phase, structural and hardness examination. Then the samples were polished with various grit size papers followed by which Murakami's etching solution was used to reveal the structure. Hardness examination was performed to analyze the variations from base material to the treated region. As per the ASTM G99-05 standard, wear test was carried out using a pin-on-disc wear machine (Made by M/S Ducom, India) [22]. The counterpart was made up of hardened steel with 100 mm diameter and 6 mm thickness.

Table 1 Chemical composition of NCI (SG 450-10)

Element	Fe	C	Si	Mn	P	S	Mg	Cr	Cu
Wt (%)	Bal.	3.69	3.16	0.610	0.0620	0.0220	0.0280	0.0350	0.218

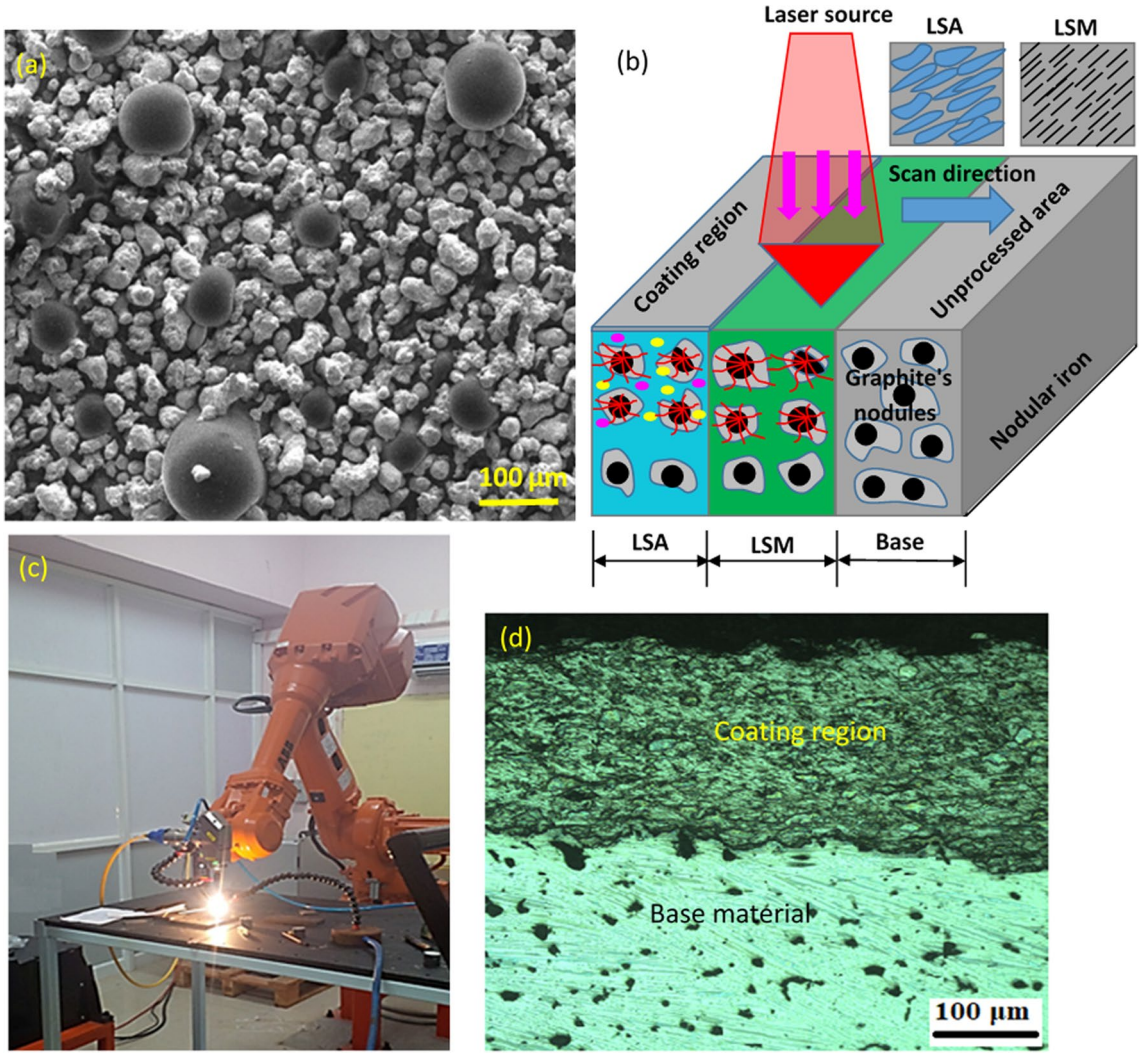

Fig. 1 Micrograph of Ni–Cr alloy powder (**a**), schematic of different laser processing with nodule softening (**b**), experimental setup used in this study with six-axis robot (**c**), micrograph of preplaced Ni–Cr coating with thickness (**d**)

Table 2 Optimized laser parameters

Specimen	Laser power (kW)	Scan speed (mm/min)	Overlapping (%)	Defocus (mm)
NCI	1.5	600	30	15

The mass loss of the pin was measured using a weighing machine after every wear test. Besides, worn out surface was analyzed to study the wear mechanism using scanning electron microscopy (SEM). The average roughness of worn-out samples was measured using white-light interferometer (Made of M/S Rtec, USA).

3 Results and discussion

3.1 Microstructural examination

The structure of the as-received NCI is shown in Fig. 2a, b. From the micrograph, maximum amount of ferrite with lesser content of pearlite can be observed in the matrix. The metallographic investigation revealed that the analyzed NCI has 12% graphite, 6% pearlite and 82% ferrite content in the matrix. The nodule graphites which have 76% nodularity and 50 µm size were distributed evenly in the cast material. The measured base material hardness was 220 $HV_{0.3}$. Figure 3a shows the partially melted region and a transition region between the alloyed layer. It can be observed that the partially melted region shows a eutectic ledeburite structure. In partially melted region, most of the nodules were completely dissolved during the LSA

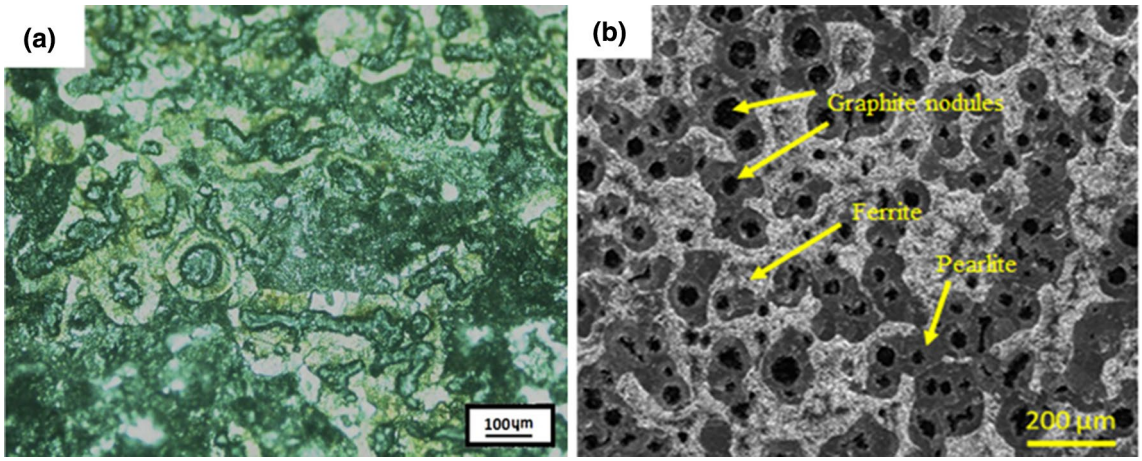

Fig. 2 Optical micrograph of nodular iron (**a**), scanning electron micrograph showing graphite nodules with ferrites (**b**)

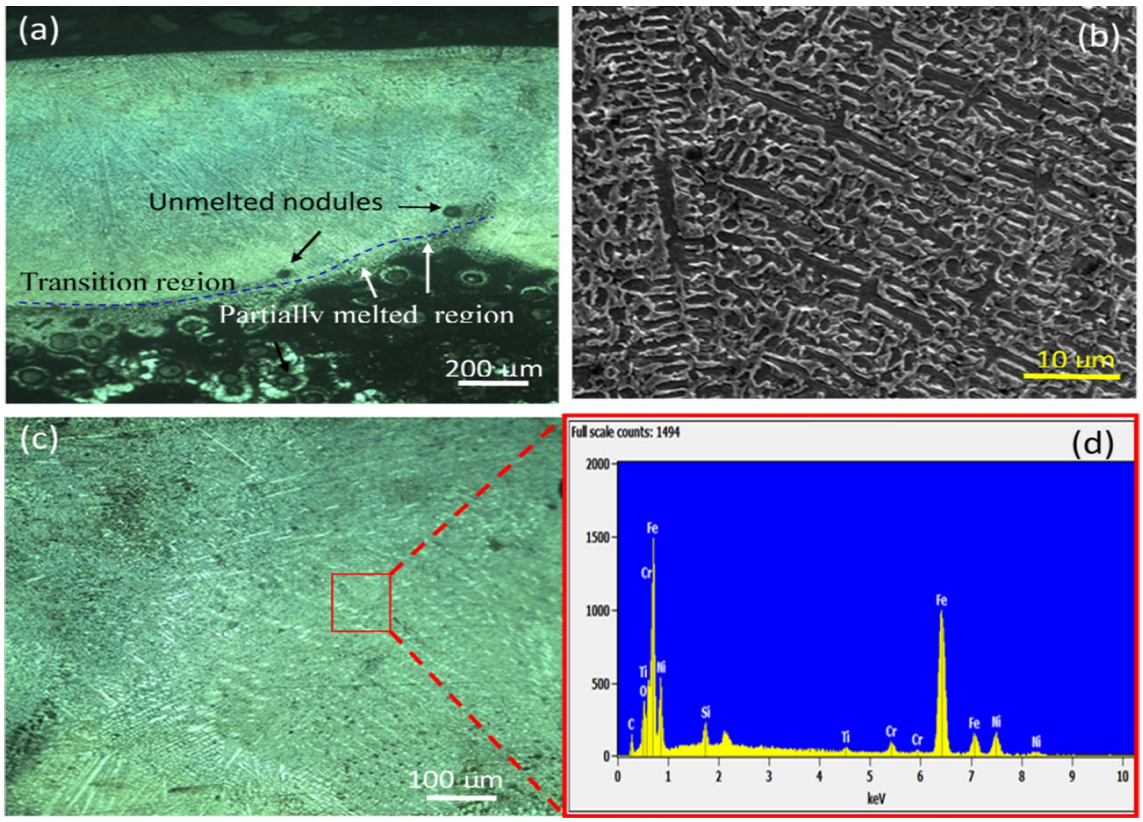

Fig. 3 Optical micrograph of laser-alloyed cross section (**a**), SEM of laser-alloyed region with dendrite structure (**b**), micrograph and corresponding elemental results (**c**, **d**)

process. Hence, the partially melted region shows higher carbon content due to the rapid cooling rate of alloying, and coarser carbide elements can be solidified directly from the liquid as an outcome of the eutectic reaction. This can create a strong brittle network along the alloyed fusion line.

Figure 3a represents the heat-affected region with a higher percentage of martensite with some un-melted nodules. In alloying periods, heat-affected region delivers higher temperatures compared to eutectoid temperature in the iron–carbon phase diagram [10]. Therefore, the graphite nodules start to dissolve in the austenite (γ-Fe) during higher

temperatures and then change into martensite (M-phase) because of a higher rate of cooling [23]. Figure 3b, c shows the SEM and optical micrograph (OM) images of cross-sectioned alloying layers. The structure occurs as hypoeutectic which is composed of ledeburite and pre-eutectic austenite. Further, it shows the normal transformation of γ-phase (austenite) to M-phase (martensite) on NCI. The laser alloyed cross section shows the fine microstructure and exhibited a defect-free surface. The γ-phase contained higher percentage of Ni element than cementite (Fe_3C), while the Fe_3C phases more Cr and less Ni element. Hence, the presence of Fe_3C on the laser-alloyed surface was rich in Cr and the γ-phase was supported through the solid solution of both alloy powders of Ni and Cr. Also, the fine microstructure was formed on the laser-alloyed surface due to the rapid solidification.

Figure 3d shows the elemental analysis of the alloying region. A significant increase in Cr and Ni elements was observed while compared with the original composition of the base material. Therefore, this LSA process can make significant microstructure changes on the NCI surface. Besides, elemental analyses show that γ-phase has higher Ni content than Fe_3C on the LSA surface. Further, Fe_3C comprises a maximum of Cr with less Ni content. Hence, the Fe_3C in the LSA surface is the alloyed Fe_3C rich in Cr and γ-phase is strengthened through solid solution of Cr and Ni contents. Besides, refined microstructure was noticed on the laser-alloyed surface due to rapid solidification. Also, the microhardness of the alloying region shows a significant increase by refined grain size and strengthening of both alloying elements [24].

Figure 4a shows the cross section of laser-melted NCI with partially melted nodules at the interface. The laser-treated region exhibited γ-phase dendrites with an interdendritic carbide structure as shown in Fig. 4b, c. The continuous laser exposure provides rapid heating and solidification to form the structure of the dendrite. The formed dendrites were evenly dispersed by having an interdendritic carbide structure with γ-phase [25].

After laser processing, the microstructure exhibited needle-like interdendritic structure comprised of Fe_3C

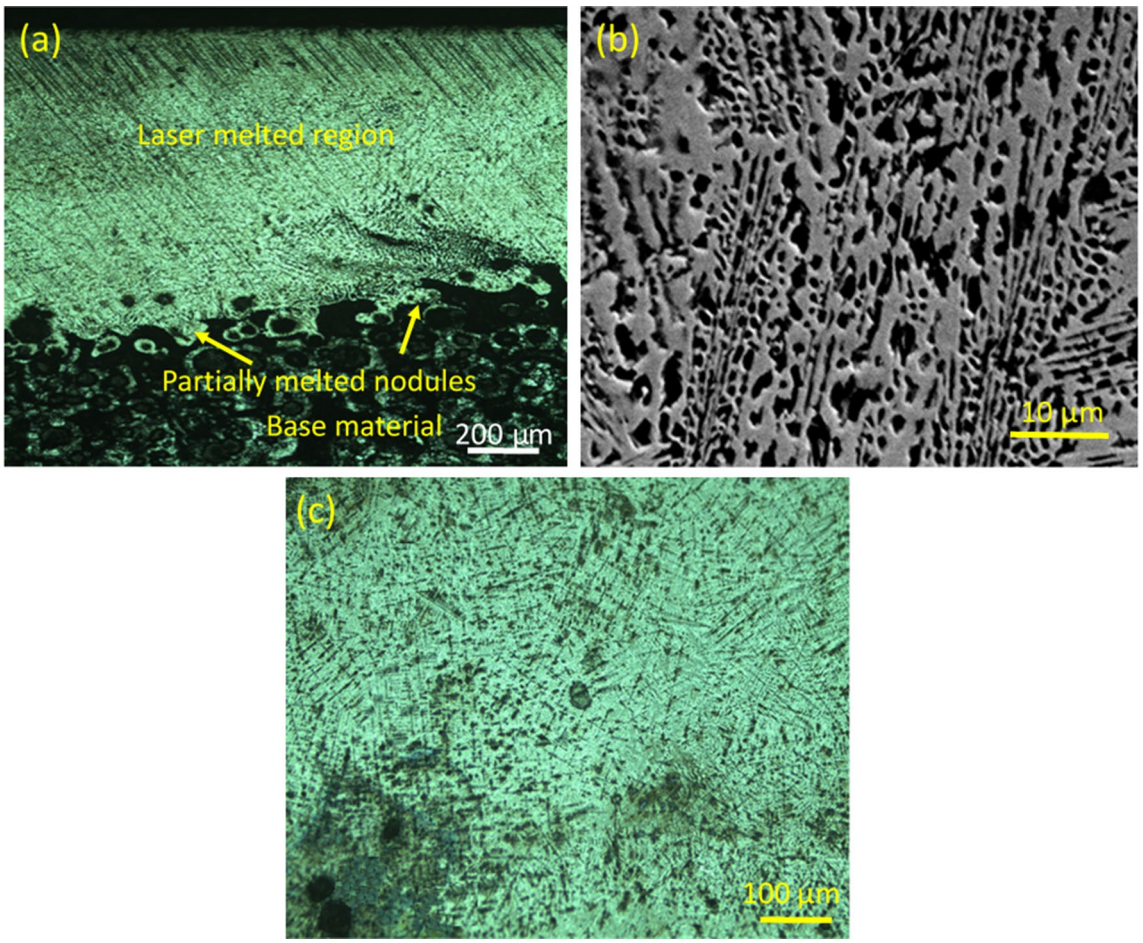

Fig. 4 Optical micrograph of laser-melted cross section (**a**), SEM of laser-melted region with dendrite structure (**b**), micrograph shows with various structure (**c**)

and M-phase having an arm space below 7 µm due to a higher cooling rate. The induced convection resulted in the formation of homogeneous dendritic. The SEM images revealed that the nodular graphite was softened during the heat treatment and the fast self-quenching paved way for the partial dissolution of nodular graphite present in the bottom layer which reduced the diameter of the nodules. The intermediate layer exhibited the presence of uneven martensite and dendrite phases. The uneven distribution of the phases explained the rapid re-solidification of the melt pool under the raster scanning of the laser beam under optimum laser parameters. The bottom region of the laser-melted zone contained a fine martensite structure. Moreover, the treated depth was free from cracks and voids. Figure 5 indicates the schematic representation of the microstructure evolution process: (a) as-received cast iron with nodules count, (b) after the alloying process (nodules dissolved), and (c) after LSM with disappeared graphite's.

3.2 Microhardness evolution

The microhardness test was performed across the laser processed depth which is shown in Fig. 6a. The increase in the hardness across the melted depth was attributed to the induced residual stress, precipitation hardening and through the refinement of grains imparted by rapid re-solidification. The optimized interaction time was induced lower thermal gradient and the higher cooling rate which is favored the refinement of grains across the treated depth. The presence of finely refined grains has increased the hardness in the laser-treated zone. Figure 6a shows the level of melt depth (~900 µm) which was achieved through LSM. The treated depth exhibited an average hardness of 880 $HV_{0.3}$ which was four times greater than the substrate material. The uniform microhardness values were obtained due to homogeneous grain structure. The partially melted region shows the maximum hardness of 920 $HV_{0.3}$ which is attributed to the insufficient melting of graphite nodules and the creation of fine ledeburite microstructure along with the graphite interface.

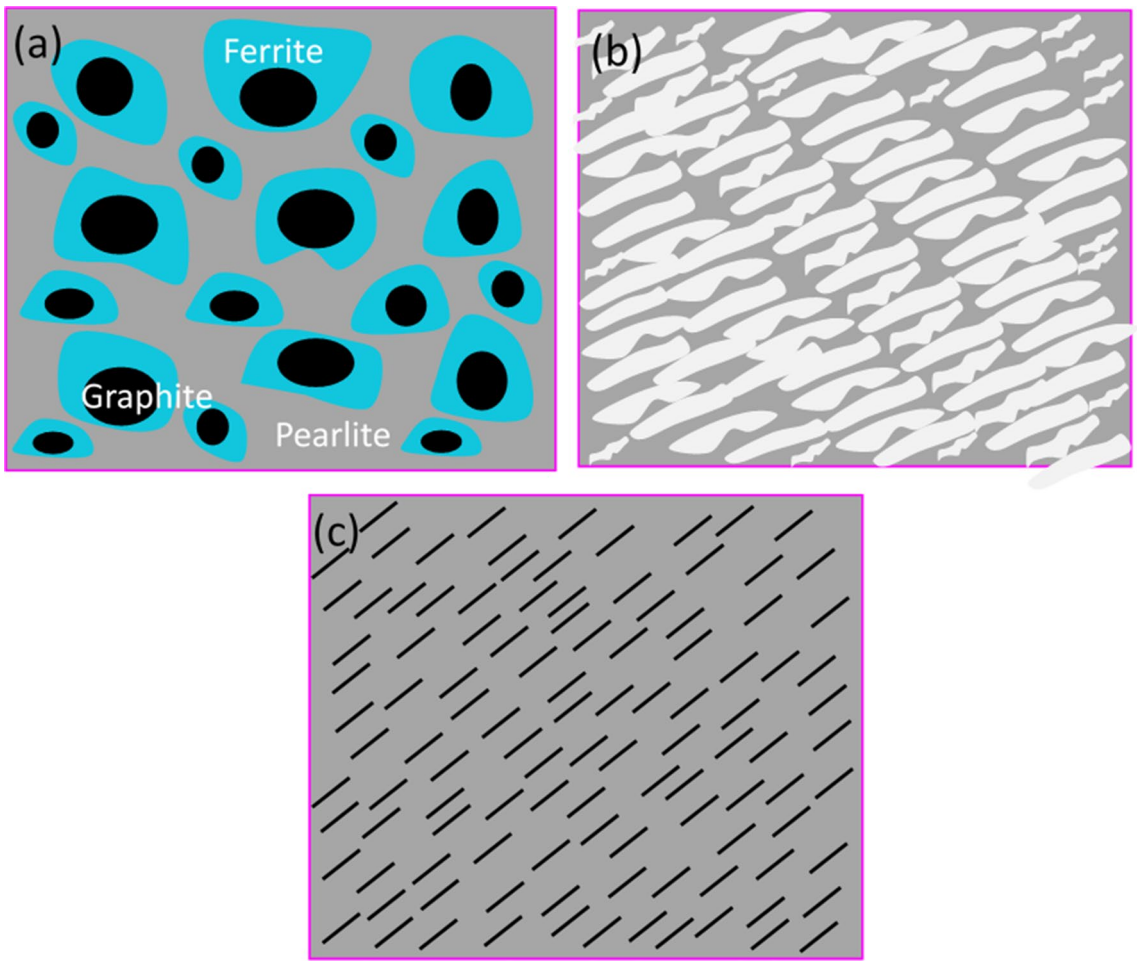

Fig. 5 Schematic representation of evolution process: (**a**) as-received cast iron with nodules count, (**b**) after alloying process (nodules dissolved), (**c**) after laser melting with disappeared graphite

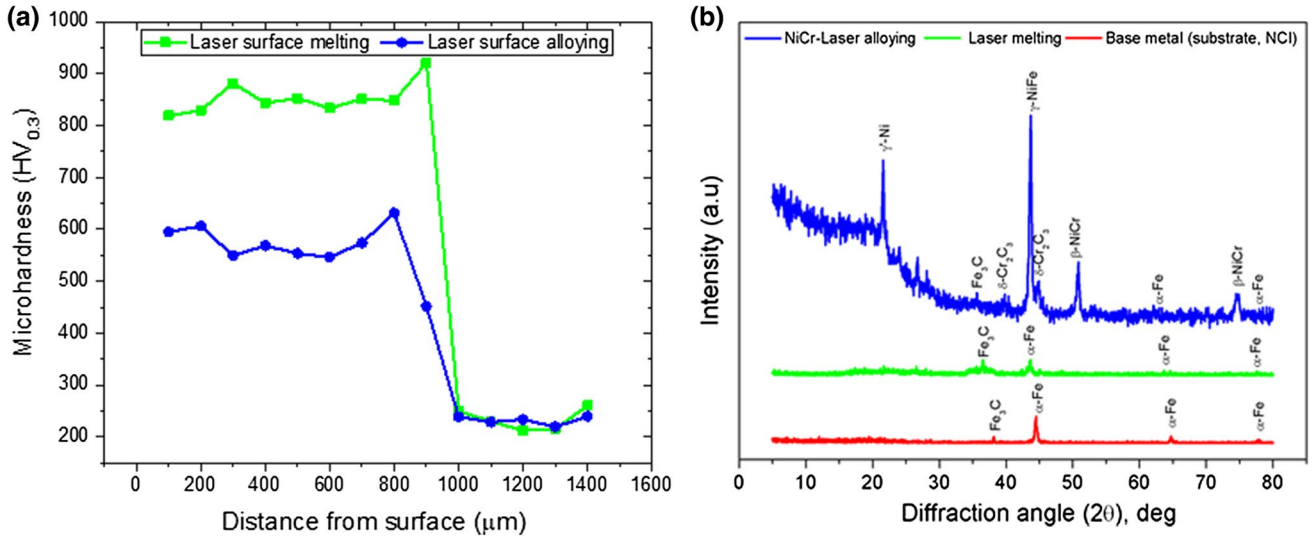

Fig. 6 Microhardness analyses of laser treated cross section (**a**), phase analyses of base material and laser-processed samples (**b**)

The laser-alloyed region indicates significant increases in hardness with a depth of ~ 850 μm. The alloyed layer was strengthened by both the refined grain sizes and hard alloying elements. The laser-alloyed surface shows the average hardness of ~ 578 $HV_{0.3}$ which is 2.62 times higher when compared to the substrate material. Practically it is proved that while hard alloy powders penetrate the substrate surface, the hardness of the base material was improved. Also, the same author has noticed the similiar trend of results with alloying of hard powders and improved the base material hardness [26]. After LSA with Ni–20% Cr, the hardness was enhanced 2.62 times due to grain size refinement. Also, needle-like produced microstructure showed better reinforcement to the alloyed region.

3.3 Phase analyses

The phase analyses of the substrate, LSM, and LSA surfaces are shown in Fig. 6b. The observed XRD peaks on the base material were related to α-Fe and Fe_3C phases. After LSM, the same two different phases, namely α-Fe and Fe_3C phases were noticed. These results explained that the γ-phase was retained after LSM. However, observed peaks were shifted to lower diffraction angle and intensity of the α-Fe phase was decreased and broadened. These results demonstrated clearly that severe distortion has occurred in the α-Fe lattice and grain refinement has occurred in the substrate. Hence, the hardness of the laser-melted surface showed higher value when compared to the substrate. Further, the observed hard Fe_3C phase in laser melting was more than the base material due to which the hardness of laser-melted surface also resulted in a higher value. Due to rapid heating and cooling, more amount of hard Fe_3C phase was expected to form which was pinned the α-Fe grains (grain refinement). The laser-alloyed sample exhibited six different phases, namely α-Fe, β-NiCr, γ-NiFe, γ′-Ni, δ-Cr_2C_3 and Fe_3C phases. These results indicated that the alloying of NiCr was attained by the LSA technique. These solid solutions of β-NiCr and γ-NiFe phases, the third hard phase of δ-Cr_2C_3 and Fe_3C in the substrate were expected to increase the hardness compared to base metal [27].

3.4 Wear and friction behavior

Normally, studying the wear process is a little difficult which is comprises several conditions such as atmosphere, properties, and type of loading [28]. The selected wear study parameters are 30 N load, 1.5 m/s sliding velocity and 2000 m sliding distance. The mass loss of base material is higher when compared to laser-processed specimens as shown in Fig. 7a. The results showed that mass loss of base material is around 445 mg while the laser-processed sample shows 90 mg (LSM) and 135 mg (LSA) for the sliding distance of 2000 m. The reason for less material removal is improved material hardness of base material after laser processing. Moreover, as the sliding distance was increased, the weight loss also kept on increasing for the substrate material. The mass loss of the laser-processed samples is minimal at the beginning of the experiment and maintains the same trend for the complete experiment.

Figure 7b shows the coefficient of friction (CoF) of base material and laser-processed samples. The substrate CoF is high as 0.8 at the initial stage of the experiment and then decreases to ~ 0.5 and maintains stability. After the initial fall, the CoF was increased gradually because the contact of pin and disc have produced considerable friction. Further,

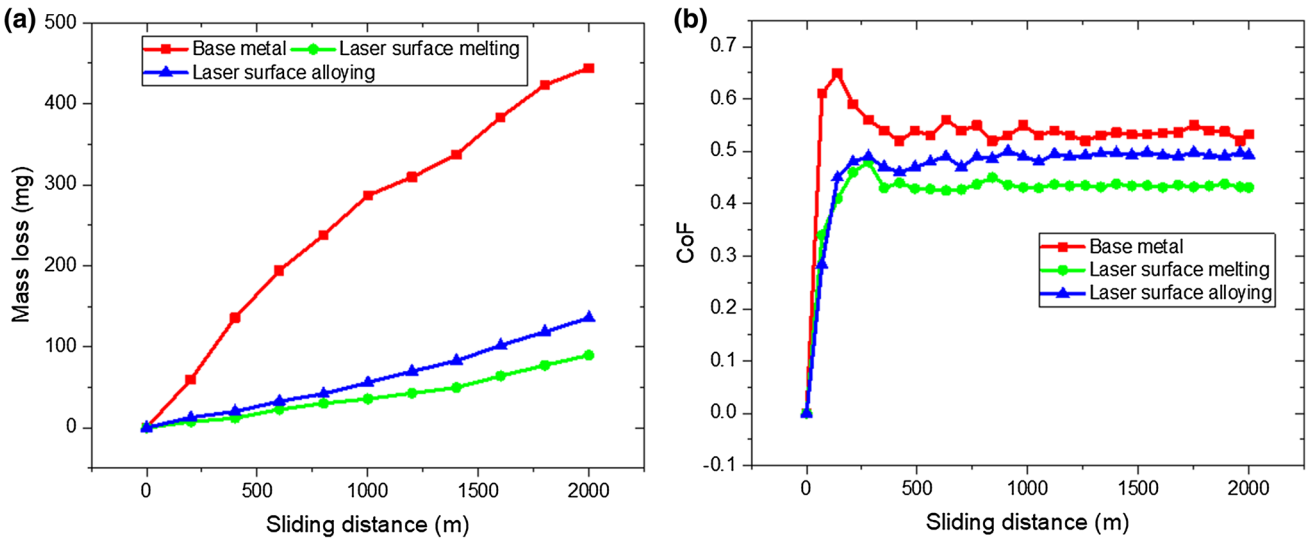

Fig. 7 Mass loss (**a**) and friction coefficient (**b**) for base material and laser-processed samples

these contact surfaces have started to progress into the self-mating stage which has resulted in more area touches between the counterpart and pin. Therefore, the friction force increased and consequently the CoF also increased. The CoF of laser-melted specimen and laser-alloyed specimen is shown to be approximately 0.43 and 0.49, respectively. The substrate CoF was more than that for the laser-treated samples. These results were expected to be the higher hardness of surfaces which is altered by laser processing. Further, these improved strengths over the surface were caused in the lower area of contact. Hence, the lesser sum of contact points was noticed which is expected to need lesser input energy for getting sheared in sliding [29]. The friction has produced heat through sliding contact which led to an increase in temperature and forms the oxides on the surfaces. This oxide formation has protected the surfaces from the wear which also reduced the friction [30–32]. However, the CoF is increased in LSA while compared to the LSM sample due to lower strength [33, 34]. The presence of M-phase, δ-Cr_2C_3 and Fe_3C also induced the higher friction between the mating surfaces [35].

3.5 Wear mechanism and its roughness

SEM and corresponding white light interferometer images were taken to analyze the wear debris, wear track and surface roughness of base material, LSM and LSA samples to study the possible wear mechanisms. The wear rate and wear mechanism may differ based on the material. However, adhesion could have occurred between two sliding parts due to plastic deformation. Similarly, the produced wear debris might be admixed, agglomerated and retained in the wear track. Further, those wear debris penetrate into specimen surface under applied load and produce the damages for the sample surface through plowing and cutting due to reciprocating motion [36].

Figure 8a–c represents the wear track of base material and laser-processed surface by showing the delamination and adhesive particles. The delamination concept represents the plastic deformation, crack opening and it will spread over the specimen surface and leads to debris lamination. It can be noticed that plow marks are visible on the tested base material surface and severe plastic deformation was observed due to poor wear resistance. In addition, series deformation and several patches of adhesives, longitudinal grooves spreading along the sliding movement were noticed on the worn-out substrate surface (Fig. 8a). This kind of damages proves that as-received NCI suffered severe adhesive wear. The corresponding average surface roughness of worn-out base material is shown in Fig. 9a. A maximum roughness of 6.2 µm was noticed on the worn-out surface of the base material. This is due to lower hardness with the high-temperature atmosphere at the contact surfaces and less resistance to material loss. While the pin surface is in contact with counterpart surface during the dry wear test, the contact point of the local temperature was higher and the hardness of around these points decreased immediately. As an outcome, severe plastic deformation and serious metal transfer from the mating surfaces were observed [37].

Figure 8b shows the worn-out surfaces of LSA specimens. The observed wear track is smoother with less deformation compared to a base material. The tested laser-alloyed surface shows more damages and plowing of metals compared to laser-melted specimens. However, the laser alloying surface controlled the material loss due to the deposition of harder Ni–Cr particles. While laser-alloyed pin surfaces

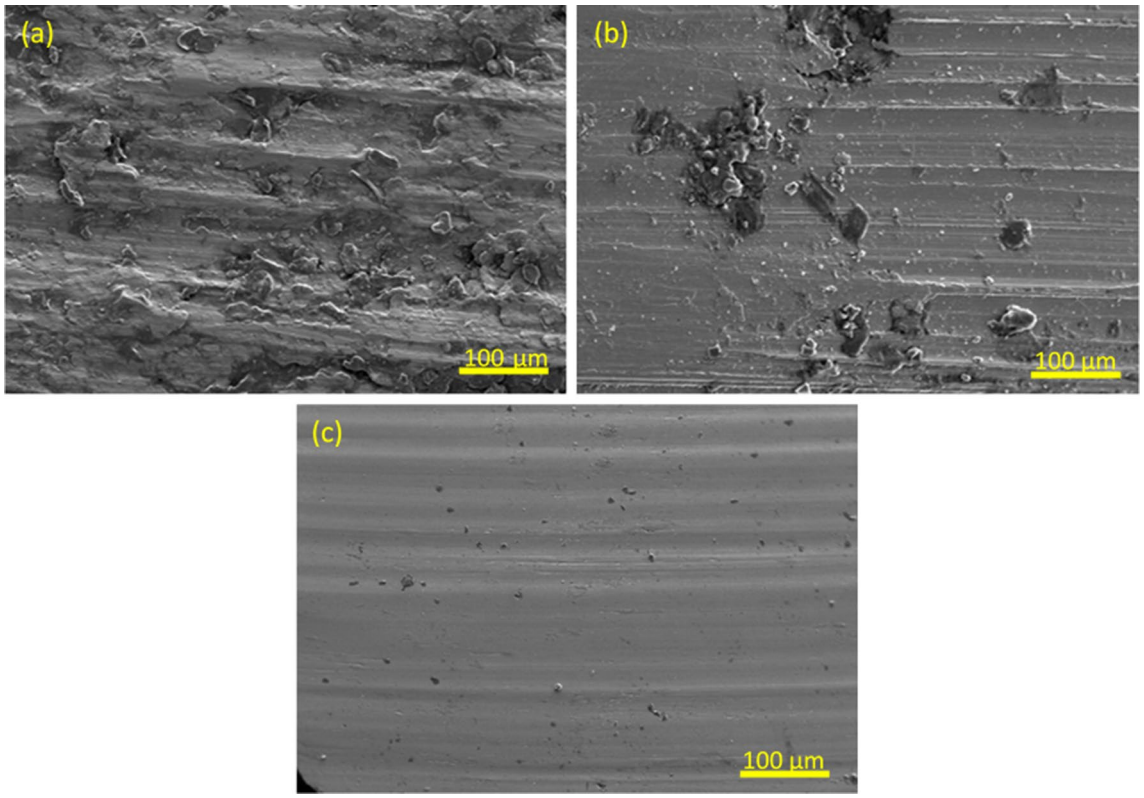

Fig. 8 Worn-out surface of base material (**a**), laser-alloyed (**b**), laser-melted specimen (**c**)

touch the disc surface, the harder surface of the counter-body (disc) pressed the laser-alloyed surface with a high load. As a consequence, the material was removed from the pin surface by adhesion mechanism [38]. The pull-out material and depth of wear track on the pin surface were reasonable compared to the base material. The elongated eutectic carbides controlled the material loss and enhanced the wear resistance by providing nominal hardness. In addition, a rapidly solidified homogeneous structure offers LSA layers with the combination of good wear resistance with improved hardness. Also, some oxide particles were observed on the worn-out laser-alloying surface and it protected some material loss from the laser-alloying region. The worn-out surface of the laser-alloying specimen shows the average surface roughness of 3.3 µm as shown in Fig. 9b. The wear rate was improved moderately due to the alloying of harder particles into the base material surface. Hence, the roughness of the laser-alloying specimens was lesser than the base material.

In Fig. 8c, the wear track of the LSM specimen is presented. The noticed wear track indicates smooth and less material loss on the LSM surface. However, some minor grooves and delamination can be noticed on the tested surfaces. The worn-out surfaces show fewer scratches and deformation compared to the base material and laser-alloyed sample. The wear depth and pile-up material were less on the melted region as it shows finer groves on the melted worn out surfaces. These finer grooves indicate that wear resistance of the material was increased due to microstructure changes with improved hardness. Also, laser-melted surface shows higher wear resistance than base metal and laser-alloyed sample due to refined grain structure. The occurrence of fine M-phase and retained γ-phase along with the hard phase of Fe_3C play a vital role in wear resistance enhancement. Among all the samples, LSM worn-out surfaces (Fig. 9c) are finer and shallower than the other two surfaces. The reason for this behavior is the worn-out debris particle is not able to penetrate the surface because of the higher microhardness of the LSM sample. The corresponding average surface roughness of worn-out laser melting surface around 1.9 µm is shown in Fig. 9c. This average surface roughness was lesser than base material and laser-alloyed samples due to improved wear resistance and microhardness. The delaminated particles are very less on worn-out surface of the LSM sample compared to the other two samples. This proves that minor abrasion is the major predominant wear mechanism in LSM specimens while adhesion and plowing are the major ones for the other two specimens. Figure 10 shows the schematic representation of various wear mechanisms.

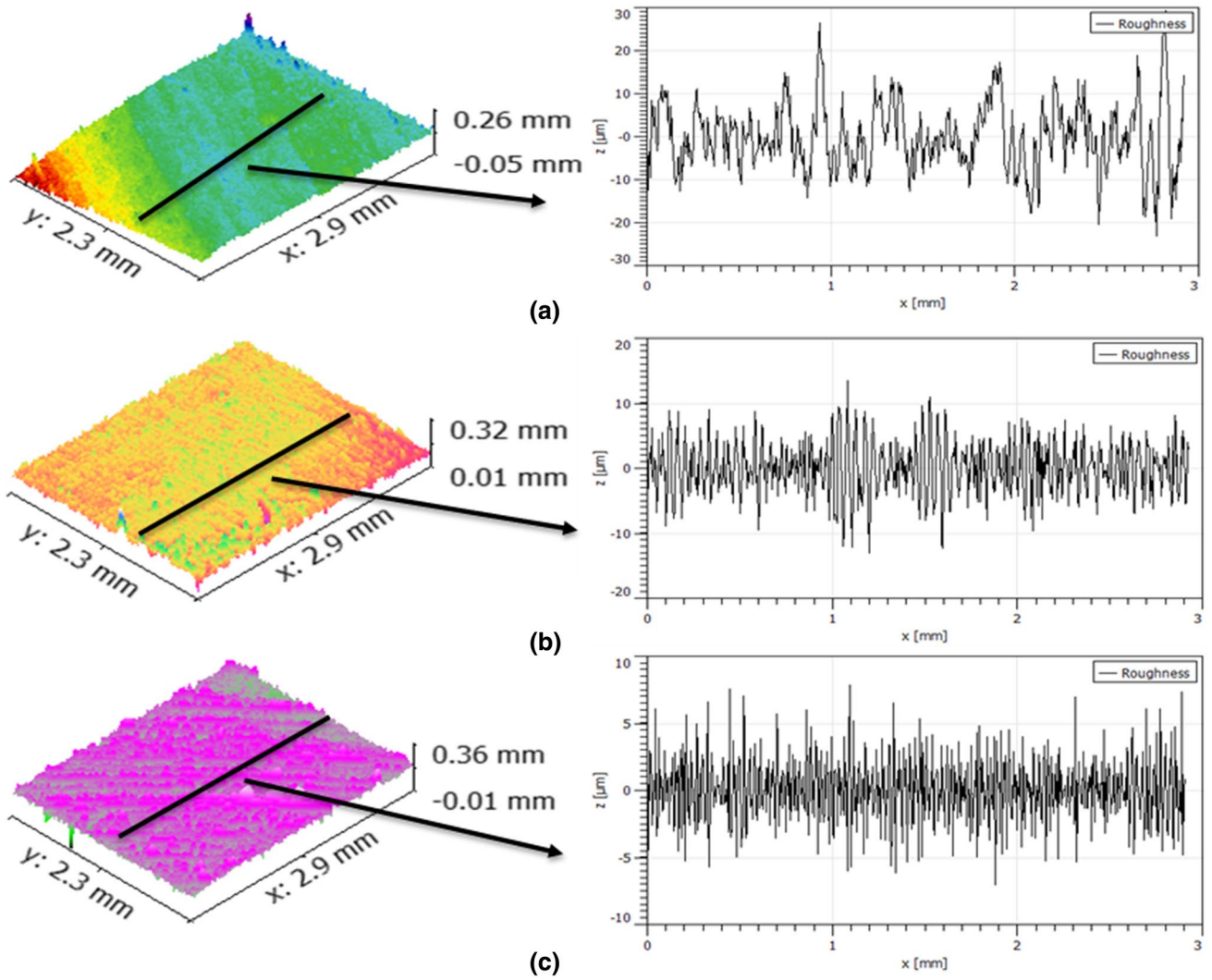

Fig. 9 Surface roughness of worn-out pin: (**a**) base material, (**b**) laser-alloyed specimen, (**c**) laser-melted specimen

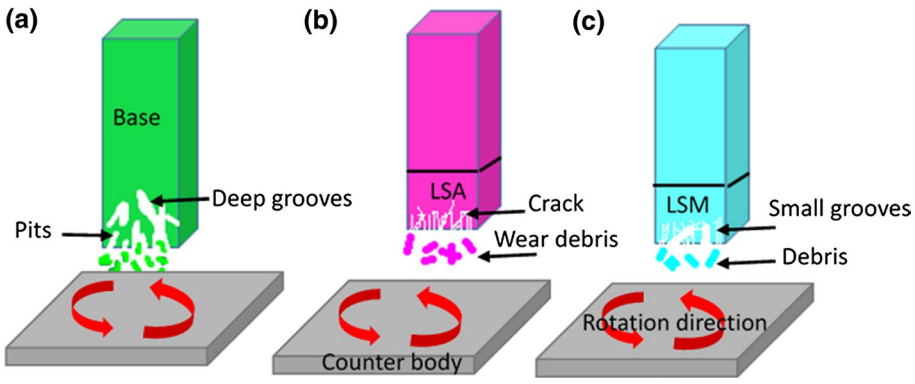

Fig. 10 Schematic representation of various wear mechanism: base material shows deep grooves with pits (**a**), alloyed sample indicates the crack initiation with debris (**b**), laser-melted specimen with small grooves (**c**)

4 Conclusion

The advanced manufacturing process of LSM and LSA was applied successfully on the NCI. Further, the improvement in the microhardness and wear resistance was investigated. Based on the tribo-characterization results, the following points can be drawn:

- The laser-alloyed microstructure is hypoeutectic which is composed of ledeburite and pre-eutectic austenite with the normal transformation of γ-phase to M-phase. The laser-melted region exhibited γ-phase dendrites with an interdendritic carbide structure. Moreover, both laser-processed samples were free from cracks and voids.
- The optimized interaction time induced a lower thermal gradient and the higher cooling rate which favored the refinement of grains and improved the hardness. After LSM, α-Fe and Fe_3C phases were noticed while laser-alloyed sample exhibited α-Fe, β-NiCr, γ-NiFe, γ′-Ni, δ-Cr_2C_3 and Fe_3C phases.
- The mass loss of base material is higher while compared to laser-processed specimens due to lower hardness. The substrate CoF was more than that of the laser-treated samples. These results were expected to show higher hardness for surfaces which are altered by laser processing.
- The noticed wear track indicates that abrasion, adhesion and delamination were the major wear mechanisms. The laser-melted worn-out surface exhibits lesser roughness compared to the substrate (4.3 times) and laser-alloyed specimen (1.4 times).
- In comparison, laser-melted surface shows higher wear resistance than the laser-alloyed samples due to refined grain structure. The occurrence of fine martensite and retained austenite along with the hard phase of Fe_3C play a vital role in wear resistance enhancement.

Acknowledgements Authors wish to thank National Taipei University of Technology, Taiwan (Republic of China), and National Institute of Technology, Tiruchirappalli, India, for all support to carry out this research work.

Data availability statement The experimental datasets obtained from this research work and then the analyzed results during the current study are available from the corresponding author on reasonable request.

Compliance with ethical standards

Conflict of interest The authors declare no conflict of interest.

References

1. Medyński D, Janus A. Effect of heat treatment parameters on abrasive wear and corrosion resistance of austenitic nodular cast iron Ni–Mn–Cu. Arch Civ Mech Eng. 2018;18:515–21.
2. Alabeedi KF, Abboud JH, Benyounis KY. Microstructure and erosion resistance enhancement of nodular cast iron by laser melting. Wear. 2009;266:925–33.
3. Podgornik B, Vizintin J, Thorbjornsson I, Johannesson B, Thorgrimsson JT, Celis MM, Valle N. Improvement of ductile iron wear resistance through local surface reinforcement. Wear. 2012;274:267–73.
4. Roy A, Manna I. Laser surface engineering to improve wear resistance of austempered ductile iron. Mater Sci Eng A. 2001;297:85–93.
5. Fauchais P, Montavon G. Plasma spraying: from plasma generation to coating structure. Adv Heat Transf. 2007;40:205–344.
6. Sohi MH, Ebrahimi M, Ghasemi HM, Shahripour A. Microstructural study of surface melted and chromium surface alloyed ductile iron. Appl Surf Sci. 2012;258:7348–53.
7. Yasavol N, Abdollah-Zadeh A, Ganjali M, Alidokht SA. Microstructure and mechanical behavior of pulsed laser surface melted AISI D2 cold work tool steel. Appl Surf Sci. 2013;265:653–62.
8. Yilbas BS, Patel F, Karatas C. Laser controlled melting of HSLA steel surface with presence of B4C particles. Appl Surf Sci. 2013;282:601–6.
9. Jeyaprakash N, Duraiselvam M, Raju R. Modelling of Cr_3C_2-25% NiCr laser alloyed cast iron in high temperature sliding wear condition using response surface methodology. Arch Metall Mater. 2018;63:1303–15.
10. Shamanian M, Abarghouie SMRM, Pour SRM. Effects of surface alloying on microstructure and wear behavior of ductile iron. Mater Des. 2010;31:2760–6.
11. Majumdar JD, Manna I. Laser surface alloying of AISI 304-stainless steel with molybdenum for improvement in pitting and erosion–corrosion resistance. Mater Sci Eng A. 1999;267:50–9.
12. Christodoulou G, Walker A, Steen WM, West DRF. Laser surface melting of some alloy steels. Met Technol. 1983;10:215–23.
13. Kim Y-W, Strutt PR, Nowotny H. Laser melting and heat treatment of M2 tool steel: a microstructural characterization. Metall Trans A. 1979;10:881–6.
14. Abbaschian R, Abbaschian L, Reed-Hill RE, Abbaschian R. Physical metallurgy principles. 4th ed. Cengage Learning (2009).
15. Abboud JH, West DRF. Laser surface melting of Ti-10 V-2Fe-3Al alloy. J Mater Sci Lett. 1992;11:1322–6.
16. Zhong M, Liu W, Zhang H. Corrosion and wear resistance characteristics of NiCr coating by laser alloying with powder feeding on grey iron liner. Wear. 2006;260:1349–55.
17. Staia MH, Cruz M, Dahotre NB. Microstructural and tribological characterization of an A-356 aluminum alloy superficially modified by laser alloying. Thin Solid Films. 2000;377:665–74.
18. Tomlinson WJ, Bransden AS. Cavitation erosion of laser surface alloyed coatings on Al-12% Si. Wear. 1995;185:59–65.
19. Majumdar JD, Mordike BL, Manna I. Friction and wear behavior of Ti following laser surface alloying with Si, Al and Si + Al. Wear. 2000;242:18–27.
20. Lo KH, Cheng FT, Kwok CT, Man HC. Improvement of cavitation erosion resistance of AISI 316 stainless steel by laser surface alloying using fine WC powder. Surf Coat Technol. 2003;165:258–67.
21. Tjong SC, Ku JS, Ho NJ. Laser surface alloying of ferritic Fe-40Cr alloy with ruthenium. Surf Coat Technol. 1997;90:203–9.
22. G. ASTM, 99-05, Stand. Test method wear test with a Pin-on-Disk Appar. 2010; 1–5.

23. Jeshvaghani RA, Harati E, Shamanian M. Effects of surface alloying on microstructure and wear behavior of ductile iron surface-modified with a nickel-based alloy using shielded metal arc welding. Mater Des. 2011;32:1531–6.
24. Jeyaprakash N, Yang C-H, Duraiselvam M, Prabu G. Microstructure and tribological evolution during laser alloying WC-12% Co and Cr_3C_2-25% NiCr powders on nodular iron surface. Results Phys. 2019;12:1610–20.
25. Jeyaprakash N, Yang C-H, Duraiselvam M, Prabu G, Tseng S-P, Kumar DR. Investigation of high temperature wear performance on laser processed nodular iron using optimization technique. Results Phys. 2019;15:102585.
26. Jeyaprakash N, Duraiselvam M, Aditya SV. Numerical modeling of WC-12% Co laser alloyed cast iron in high temperature sliding wear condition using response surface methodology. Surf Rev Lett. 2018;25:1950009.
27. Sun G, Zhang Y, Liu C, Luo K, Tao X, Li P. Microstructure and wear resistance enhancement of cast steel rolls by laser surface alloying NiCr–Cr_3C_2. Mater Des. 2010;31:2737–44.
28. Buchanan VE, Shipway PH, McCartney DG. Microstructure and abrasive wear behaviour of shielded metal arc welding hardfacings used in the sugarcane industry. Wear. 2007;263:99–110.
29. Yan H, Wang A, Xiong Z, Xu K, Huang Z. Microstructure and wear resistance of composite layers on a ductile iron with multi-carbide by laser surface alloying. Appl Surf Sci. 2010;256:7001–9.
30. Ahmed R, Ali O, Faisal NH, Al-Anazi NM, Al-Mutairi S, Toma F-L, Berger L-M, Potthoff A, Goosen MFA. Sliding wear investigation of suspension sprayed WC–Co nanocomposite coatings. Wear. 2015;322:133–50.
31. Rajinikanth V, Venkateswarlu K. An investigation of sliding wear behaviour of WC–Co coating. Tribol Int. 2011;44:1711–9.
32. Yang Q, Senda T, Ohmori A. Effect of carbide grain size on microstructure and sliding wear behavior of HVOF-sprayed WC–12% Co coatings. Wear. 2003;254:23–34.
33. Sugishita J, Fujiyoshi S. The effect of cast iron graphites on friction and wear performance: II: variables influencing graphite film formation. Wear. 1981;68:7–20.
34. Gadag SP, Srinivasan MN. Dry sliding wear and friction: laser-treated ductile iron. Wear. 1994;173:21–9.
35. Pagano N, Angelini V, Ceschini L, Campana G. Laser remelting for enhancing tribological performances of a ductile iron. Procedia CIRP. 2016;41:987–91.
36. Kumar S, Mondal DP, Jha AK, Khaira HK. Improvement in high stress abrasive wear property of steel by hardfacing. J Mater Eng Perform. 1999;8:711–5.
37. Wang XH, Zhang M, Liu XM, Qu SY, Zou ZD. Microstructure and wear properties of TiC/FeCrBSi surface composite coating prepared by laser cladding. Surf Coat Technol. 2008;202:3600–6.
38. Velmanirajan K, Thaheer ASA, Narayanasamy R, Basha CA. Numerical modelling of aluminium sheets formability using response surface methodology. Mater Des. 2012;41:239–54.